CHALMERS

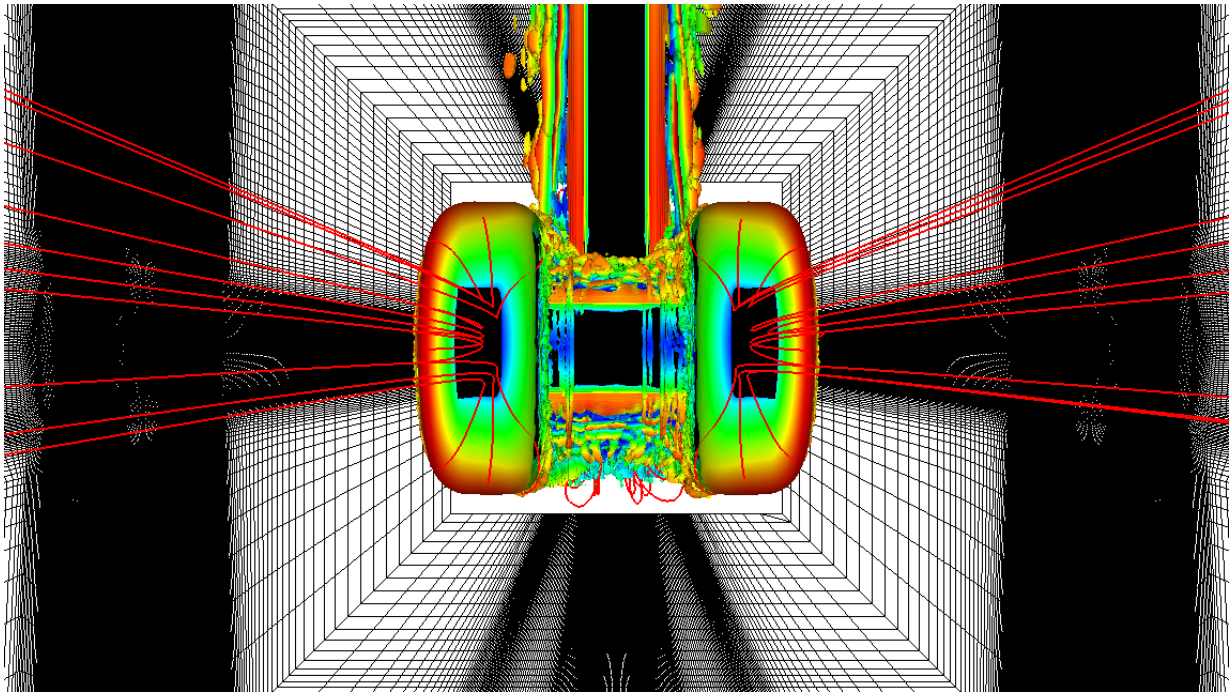

Aerodynamic Flow Simulation of a Rudimentary Landing Gear Using PANS and LES

Master's Thesis in Solid and Fluid Mechanics

RAGNAR LÁRUSSON

Department of Applied Mechanics
Division of Fluid Mechanics
CHALMERS UNIVERSITY OF TECHNOLOGY
Göteborg, Sweden 2011
Master's Thesis 2011:57

MASTER'S THESIS 2011:57

Aerodynamic Flow Simulation of a Rudimentary Landing Gear Using PANS and LES

Master's Thesis in Solid and Fluid Mechanics

RAGNAR LÁRUSSON

Department of Applied Mechanics
Division of Fluid Mechanics
CHALMERS UNIVERSITY OF TECHNOLOGY
Göteborg, Sweden 2011

Aerodynamic Flow Simulation of a Rudimentary Landing Gear Using PANS and LES
RAGNAR LÁRUSSON

Master's Thesis 2011:57
ISSN 1652-8557
Department of Applied Mechanics
Division of Fluid Mechanics
Chalmers University of Technology
SE-412 96 Göteborg
Sweden
Telephone: + 46 (0)31-772 1000

Cover:
Front view of the landing gear, an artistic representation. LES results are visualized. Red lines are velocity stream lines. Iso-surface of the second invariant of the velocity gradient is made visible and colored with velocity magnitude. The mesh on the computational domain boundaries is made visible except at the outlet in the far view.

Chalmers Reproservice
Göteborg, Sweden 2011

Aerodynamic Flow Simulation of a Rudimentary Landing Gear Using PANS and LES
Master's Thesis in Solid and Fluid Mechanics
RAGNAR LÁRUSSON
Department of Applied Mechanics
Division of Fluid Mechanics
Chalmers University of Technology

Abstract

Aerodynamic flow past a four wheel rudimentary airplane landing gear is simulated using two different simulation methods. Partially - averaged Navier - Stokes (PANS) and Large Eddy Simulation (LES). The rudimentary landing gear was specially designed for wind tunnel testing and CFD and is a "stepping stone" case within the ATAAC project, an international project that aims to improve CFD methods for flows relevant to todays aeronautical industry. In this study, PANS provides a seamless transition from k - ζ turbulence model and Direct Numerical Simulation (DNS) based on the unresolved to total kinetic energy ratio (f_k) and the unresolved to total dissipation ratio (f_ϵ). The simulation results are compared with available experimental data. PANS appears to perform better than LES on the mesh used for this study. LES predicts false separation on the front wheel outboard sides whereas PANS correctly predicts attached flow. The computational mesh is generated in ICEM CFD and all simulations are performed with AVL FIRE.

Keywords: Computational Fluid Dynamics (CFD), AVL FIRE, ICEM CFD, Partially - Averaged Navier - Stokes (PANS), Large Eddy Simulation (LES), Rudimentary Landing Gear, ζ - f, Turbulence model

Preface

In this study a flow past a rudimentary landing gear has been simulated using two different simulation methods, Partially - Averaged Navier - Stokes (PANS) and Large Eddy Simulation (LES) and the results compared with experimental data. ICEM CFD has been used for mesh generation and the simulations where performed using AVL FIRE. The work has been carried out from September 2010 to September 2011 at the Department of Applied Mechanics, Division of Fluid Dynamics, Chalmers University of Technology, Sweden and was supported by AVL List GmbH under the supervision of Professor Siniša Krajnović.

Acknowledgments

I would like to thank my supervisor Professor Siniša Krajnović for his excellent supervision. Thanks go to SNIC (Swedish National Infrastructure for Computing) for access to their resources.
Special thanks to AVL List GmbH for financial support and providing Fire licences. Dr. Branislav Basara for CFD and technical support regarding the Fire code and Albert van der Meer for help with all sorts of software related problems and his very quick replies.
I would also like to thank Eysteinn Helgason and Jan Östh for their help with everything from learning to operate the Linux OS to discussion about fluid dynamics, the universe and life itself. I also acknowledge the rest of the faculty members and other students at the Division for their help and good company.
Lastly I would like to thank my family and friends for their support over the years.
Extra special thanks to my girlfriend Jóna Marín Ólafsdóttir. She is just the best!

Göteborg September 2011
Ragnar Lárusson

Nomenclature

Roman letters

A	area
C_d	Drag coefficient
C_l	Lift coefficient
C_L, C_{f1}, C_{f2}, $C_{\varepsilon 1}$, $C_{\varepsilon 2}$, C_η, C_μ, C_τ	Constants for the $\zeta - f$ model
$C^*_{\varepsilon 1}$, $C^*_{\varepsilon 2}$	Coefficient for the PANS method
C_s	Model constant in the Smagorinsky model
C_p	Pressure coefficient
D	Landing gear wheel diameter
f	Elliptic relaxation function
f_k	Unresolved-to-total ratio of turbulent kinetic energy
f_ε	Unresolved-to-total ratio of dissipation
k	Turbulent kinetic energy
L	Length, turbulent length scale using in the $\zeta - f$ model
l^+	Wall unit, length wise direction
n^+	Wall unit, wall normal direction
P	Production of k
p	Pressure
Q	Second invariant of the velocity gradient
S_{ij}	Resolved rate of strain tensor
$\lvert\bar{S}\rvert$	Characteristic filtered rate of strain
s^+	Wall unit, span wise direction
St	Strouhal number
T_u	Time scale for the PANS method
t	Time
U	Filtered velocity in PANS
U_∞	Inlet velocity
u	Sub filter velocity in PANS
$\bar{u}$	Filtered velocity in LES
u_*	Friction velocity
V	Exact velocity in PANS
$\overline{v^2}$	Wall normal velocity scale

Greek letters

Δ	Grid cell dimension
Δt	Time step
Δx	Cell size
δ_{ij}	Kronecker delta
ε	Dissipation
ζ	Velocity scale ratio
μ	Dynamic viscosity
ν	Kinematic viscosity
ν_u	Turbulent viscosity
ν_{sgs}	Turbulent kinematic viscosity in LES
ρ	Density
$\sigma_{ku,\varepsilon u,\zeta u}$	Coefficient for the PANS model
τ	Turbulent time scale
$\tau(V_i, V_j)$	Residual stress tensor for the PANS method
τ_{ij}	Residual stress tensor in LES
$\overline{\tau}_{ij}$	Sub grid scale stress tensor
τ_w	Surface shear stress
Φ	Flow property
ω	Frequency

Abbrevations

CFD	Computational Fluid Dynamics
CFL	Courant-Friedrichs-Levy number
DNS	Direct Numerical Simulation
LES	Large Eddy Simulation
PANS	Partially-Averaged Navier-Stokes
RANS	Reynolds Averaged Navier-Stokes
RLG	Rudimentary Landing Gear
SGS	Sub-Grid Scales
SPL	Sound Pressure Level

Subscript

u	Unresolved quantity
P	First near-wall grid node
ν	Viscous expression
t	Turbulent expression

Superscript

$+$	Wall unit
$\prime$	Standard deviation

Contents

Chapter 1

Introduction

1.1 Background and Previous Work

One of the major source of a airplane airframe noise it the landing gear. Because noise from landing gear is only present during take off and landing, this has not been a big concern for airplane manufacturers in the past and therefore there exists potential for better design toward reducing noise.
The Rudimentary Landing Gear (RLG) has been a benchmark test case for Airframe Noise Computations (BANC-1) held in Stockholm in June 2010 [1] and the results from various participants were reported in Spalart and Mejia [2]. Experimental studies on the RLG case were performed at the National Aerospace Laboratories, Bangalore, India and the results reported in Ventakrishnam et al. [3]. These experimental results are used in this study to validate the computer simulations.
The designers of the model describe it as a "rudimentary" landing gear. This is done to distinguish this test case landing gear from what can be called a "simple" landing gear which in general is a ordinary landing gear "stripped" down of brake lines, wiring and other components. The rudimentary landing gear is designed specially as a test geometry for the purpose of investigating the aerodynamic features and noise generation by means of experiments and computer simulations [4].
The RLG has rectangular axles and post with sharp edges. This is different for previous landing gear studies, for example Lazos [5], in which the model has round axles and posts. The reason for the sharp edges is that for a wide range of Reynolds numbers the separation of flow occurs at the edges thus making it more Reynolds number independent. The wheels however remain round which makes the separation along the wheels circumference harder to predict.
Partially - Averaged Navier - Stokes (PANS) was originally proposed by Girimaji et al. [6] as a hybrid method that provides smooth transition from RANS to DNS where the transition is determined by unresolved to total kinetic energy ratio (f_k) and the unresolved to total dissipation ratio (f_ϵ). Girimaji used the k - ϵ turbulence model in the RANS region and more recently Basara et al. [7] have introduced the use of the more sophisticated ζ - f turbulence model and that model is used in this study.

1.2 Limitations

It is important to state that the current study does not include any significant noise analysis but rather focuses on other flow features, especially time averaged streamlines and pressure on the landing gear surface and it certainly does not attempt to improve the design of a

landing gear.
It is also good to keep in mind the very limited reference to a real airplane landing gear that the RLG has due to its simple geometry and the fact that real landing gear design is very versatile. Furthermore this study only considers flow at a zero cant angle (meaning that flow direction is straight on the landing gear) which is only the case in just before take off and touch down in real situations. This study is also limited to only one Reynolds number value whereas airplanes operate at wide range of Reynolds numbers usually much higher than the Reynolds number for this study which is $Re_D = 1 \times 10^6$ based on the wheel diameter D.
Because of the finite time frame of this thesis work, no grid dependence study is reported in this report. However, at the time of writing this, simulations on a coarser mesh are underway.

1.3 Purpose

The aim of this study is to investigate the competence of PANS for such relatively complex flow as the RLG case by means of comparing the simulation results to experimental data and results from LES (Large Eddy Simulation) on an identical mesh. The comparison between these simulation methods is not made with the intention to determine which method is better in general. It has been shown that LES predicts flow around bluff bodies well [8]. The purpose with inventing such hybrid methods as PANS is to acquire good results with less computational effort as is usually required for LES. Thus, the comparison is made to demonstrate that PANS can generate reasonable results on a moderately fine mesh for which LES fails to produce reasonable results.

1.4 Approach

The mesh was generated using ICEM CFD, simulations where performed with AVL FIRE and the results visualized in EnSight. MATLAB was used in generating pressure plots and force plots.

Chapter 2

Theory

In this study, incompressible flow as described by the Navier - Stokes equations with constant dynamic viscosity μ is considered.
In this chapter the PANS equations using ζ - f turbulence model are introduced, the large eddy simulation equations with standard Smagorinsky model are presented, a review of selected aerodynamic coefficients follows and finally a short section about the wind tunnel experiment which results are used for validation of the simulation results. This chapter only presents the equations solved in this numerical study and does not cover the solving methods or the derivations of these equations.

2.1 PANS ζ - f

A bridging method between Direct Numerical Simulation (DNS) and Reynolds - Averaged Navier - Stokes (RANS) was developed by Girimaji [9]. The benefit of this method is it can vary from resolving all scales of motion (as DNS does) to fully modeling the turbulent scales of motion (as RANS does, the modeling is referred to as averaging). Furthermore, this variation between resolving and averaging is smooth resulting in regions of Partially - Averaged Navier - Stokes (PANS). The control parameters that determine the amount of averaging are the unresolved to total kinetic energy ratio (f_k) and the unresolved to total dissipation ratio (f_ε). The RANS model used in this study is the ζ - f model presented in Hanjalić et al. [10] which is based on Durbin's elliptic relaxation concept [11].
Consider the Partially-Averaged Navier - Stokes equations, the momentum equation (2.1.1) and the continuity equation (2.1.2) for incompressible flow with constant density ρ and kinematic viscosity ν in Cartesian tensor notation

$$\frac{DU_i}{Dt} + \frac{\partial \tau(V_i, V_j)}{\partial x_j} = -\frac{1}{\rho}\frac{\partial p}{\partial x_i} + \nu \frac{\partial^2 U_i}{\partial x_j \partial x_j} \tag{2.1.1}$$

$$\frac{\partial U_i}{\partial x_i} = 0 \tag{2.1.2}$$

The exact velocity field V_i is decomposed into a partially filtered component U_i and a sub - filter component u_i

$$V_i = U_i + u_i \tag{2.1.3}$$

where $\tau(V_i, V_j)$ is the sub - filter stress resulting from partially averaging the non-linear terms in the exact momentum equation. In the ζ - f model the modeled transport equations for dissipation ε and turbulent kinetic energy k are solved along with the transport equation for the velocity scale ratio $\zeta = \overline{v^2}/k$ and an elliptic relaxation function for the quantity f (not to be confused with f_k or f_ε).

The complete set of equations describing the PANS ζ - f model are seen in equations (2.1.6) to (2.1.20). The unresolved scales are indicated by u. The control parameters f_k and f_ε have now been introduced into the ζ - f model equations. For derivation of the PANS ζ - f model see Basara et al. [7].
The unresolved-to-total ratios of kinetic energy and dissipation are defined respectively as

$$f_k = \frac{k_u}{k} \tag{2.1.4}$$

$$f_\varepsilon = \frac{\varepsilon_u}{\varepsilon} \tag{2.1.5}$$

In this study, all dissipation is modeled meaning that $f_\varepsilon = 1$ and $\varepsilon_u = \varepsilon$. The turbulent viscosity ν_u is calculated as

$$\nu_u = C_\mu \zeta_u \frac{k_u^2}{\varepsilon_u} \tag{2.1.6}$$

where C_μ is an empirical constant.
The sub - filter stress tensor is modeled using the Boussinesq assumption

$$\tau(V_i, V_j) = -2\nu_u S_{ij} + \frac{2}{3} k_u \delta_{ij} \tag{2.1.7}$$

where S_{ij} is the resolved rate of strain tensor

$$S_{ij} = \frac{1}{2}\left(\frac{\partial U_i}{\partial x_j} + \frac{\partial U_j}{\partial x_i}\right) \tag{2.1.8}$$

The modeled transport equations for the unresolved turbulent kinetic energy k_u and the unresolved dissipation ε_u read

$$\frac{Dk_u}{Dt} = P_u - \varepsilon_u + \frac{\partial}{\partial x_j}\left[\left(\nu + \frac{\nu_u}{\sigma_{ku}}\right)\frac{\partial k_u}{\partial x_j}\right] \tag{2.1.9}$$

$$\frac{D\varepsilon_u}{Dt} = C_{\varepsilon 1} P_u \frac{\varepsilon_u}{k_u} - C^*_{\varepsilon 2}\frac{\varepsilon_u^2}{k_u} + \frac{\partial}{\partial x_j}\left[\left(\nu + \frac{\nu_u}{\sigma_{\varepsilon u}}\right)\frac{\partial \varepsilon_u}{\partial x_j}\right] \tag{2.1.10}$$

where P_u is the production term

$$P_u = 2\nu_\mu S_{ij}\frac{\partial U_i}{\partial x_j} \tag{2.1.11}$$

The modeled transport equation for the unresolved velocity scale ratio ζ_u reads

$$\frac{D\zeta_u}{Dt} = f_u - \frac{\zeta_u}{k_u}P_u + \frac{\zeta_u}{k_u}\varepsilon_u(1 - f_k) + \frac{\partial}{\partial x_j}\left[\left(\nu + \frac{\nu_u}{\sigma_{\zeta u}}\right)\frac{\partial \zeta_u}{\partial x_j}\right] \tag{2.1.12}$$

Equation 2.1.12 is only valid when $f_\epsilon = 1$. Equation 2.1.13 is solved for f_u

$$L_u^2 \nabla^2 f_u - f_u = \frac{1}{T_u}\left(c_1 + C_2^{,}\frac{P}{\varepsilon}\right)\left(\zeta_u - \frac{2}{3}\right) \tag{2.1.13}$$

where

$$P = \frac{1}{f_k}(P_u - \varepsilon_u) + \frac{\varepsilon_u}{f_\varepsilon} \tag{2.1.14}$$

L_u and, T_u are the length and time scales defined from the unresolved kinetic energy and dissipation.

$$T_u = max\left[\frac{k_u}{\varepsilon}, C_\tau\left(\frac{\nu}{\varepsilon}\right)^{1/2}\right] \tag{2.1.15}$$

$$L_u = C_L max\left[\frac{k_u^{3/2}}{\varepsilon}, C_\eta\left(\frac{\nu^3}{\varepsilon}\right)^{1/4}\right] \tag{2.1.16}$$

Quantities $C_{\varepsilon 1}$, $C^*_{\varepsilon 2}$ and $\sigma_{ku,\varepsilon u,\zeta u}$ are determined according to

$$C_{\varepsilon 1} = 1.4(1 + 0.045/\zeta) \tag{2.1.17}$$

$$\sigma_{ku,\varepsilon u,\zeta u} = \sigma_{k,\varepsilon}\frac{f_k^2}{f_\varepsilon} \tag{2.1.18}$$

$$C^*_{\varepsilon 2} = C_{\varepsilon 1} + \frac{f_k}{f_\varepsilon}(C_{\varepsilon 2} - C_{\varepsilon 1}) \tag{2.1.19}$$

The parameter that determines f_k is based upon the grid spacing, thus

$$f_k = \frac{1}{\sqrt{C_\mu}}\left(\frac{\Delta}{\Lambda}\right)^{2/3} \tag{2.1.20}$$

Where Δ is the grid cell spacing and $\Lambda = k^{3/2}/\varepsilon$ is the turbulent length scale. This f_k parameter is recalculated at the end of each time step and that value used for next time step to determine the filter width [7].
Table 2.1.1 shows the values of the ζ-f model constants used.

Table 2.1.1: Constants used in the ζ-f-model.

C_μ	$C_{\varepsilon 2}$	c_1	C_2'	σ_k	σ_ε	σ_ζ	C_τ	C_L	C_η
0.22	1.9	0.4	0.65	1	1.3	1.2	6.0	0.36	85

2.2 LES

In large eddy simulations the spatially filtered Navier - Stokes equations are solved

$$\frac{\partial \bar{u}_i}{\partial t} + \frac{\partial}{\partial x_j}(\bar{u}_i\bar{u}_j) = -\frac{1}{\rho}\frac{\partial \bar{p}}{\partial x_i} + \nu\frac{\partial^2 \bar{u}_i}{\partial x_j \partial x_j} - \frac{\partial \tau_{ij}}{\partial x_j} \tag{2.2.1}$$

$$\frac{\partial \bar{u}_i}{\partial x_i} = 0 \tag{2.2.2}$$

The spatial filtering implies that the filter width is completely dependent on grid spacing. The idea is that the large energy containing eddies are resolved and computed explicitly while the effect from the smaller dissipative scales on the flow field are modeled. In equation 2.2.1 appears a residual tress tensor $\tau_{ij} = \overline{u_i u_j} - \bar{u}_i\bar{u}_j$. This stress tensor is analogous to the sub-filter stress tensor seen in 2.1.1. The residual or sub grid scale (sgs) stress tensor in this study is modeled using the standard Smagorinsky model

$$\tau_{ij} - \frac{1}{3}\delta_{ij}\tau_{kk} = -2\nu_{sgs}\bar{S}_{ij} \tag{2.2.3}$$

where $\bar{S}_{ij}$ is the resolved rate of strain defined as

$$\bar{S}_{ij} = \frac{1}{2}\left(\frac{\partial \bar{u}_i}{\partial x_j} + \frac{\partial \bar{u}_j}{\partial x_i}\right) \tag{2.2.4}$$

and

$$\nu_{sgs} = (C_s\Delta)^2|\bar{S}|; \qquad |\bar{S}| = (2\bar{S}_{ij}\bar{S}_{ij})^{1/2} \tag{2.2.5}$$

2.3 A Quick Review of Selected Coefficients and Turbulent Quantities

The drag coefficient, C_d and the lift, C_l are defined as

$$C_d = \frac{F_x}{\frac{1}{2}\rho_\infty U_\infty^2 A}, \qquad C_l = \frac{F_y}{\frac{1}{2}\rho_\infty U_\infty^2 A} \tag{2.3.1}$$

where F_x, F_y are forces acting on the RLG in the x and y direction respectively and ρ_∞ and U_∞ is the free stream density and velocity. In this study A does not represent the projected frontal area of the model as is conventional when computing force coefficients but rather uses the wheel diameter squared or A =D^2. This is because within the ATAAC project this convention has prevailed. Pressure is also conveniently presented in a non dimensional form as the ratio of relative pressure to the free stream dynamic pressure

$$C_p = \frac{p - p_\infty}{\frac{1}{2}\rho_\infty U_\infty^2} \tag{2.3.2}$$

where p is the local static pressure at the point which is being evaluated and p_∞ is the free stream pressure. The viscous unit, n^+, also known as the wall unit, is a dimensionless quantity defined as

$$n^+ \equiv \frac{u_* n}{\nu} \tag{2.3.3}$$

where n is the distance normal to the surface and u_* is the friction velocity defined as

$$u_* \equiv \sqrt{\frac{\tau_w}{\rho}} \tag{2.3.4}$$

and τ_w is the surface shear stress. In order to resolve boundary layers the cells closest to the wall need to have wall distance $n^+ < 1$ to the first node.

When performing unsteady simulations it is important that flow information is transferred correctly between time steps. The time step size is limited to CFL number below one, i.e

$$CFL = \frac{U\Delta t}{\Delta x} \leq 1 \tag{2.3.5}$$

Physically, this criteria states that a fluid particle, traveling at speed U should not travel through more than one grid cell during on time step. This applies in general but in order to compromise between accuracy and simulation time it is acceptable that the CFL number exceeds unity in few small areas in the flow field. This is possible since the solver used in this study solves the flow equations implicitly whereas in an explicit solver this criteria must be met.
Sound pressure level (SPL) is a measure of acoustic pressure fluctuation intensity, p_{rms}, relative to some reference pressure, p_{rev}, which is usually taken as $p_{rev} = 2 \cdot 10^{-5}$Pa which is the threshold of human hearing at 1 Hz. The SPL is defined as

$$SPL = 20 \log_{10}\left(\frac{p_{rms}}{2 \cdot 10^{-5}}\right) \tag{2.3.6}$$

In this study, the SPL is investigated in frequency space. The time history of the pressure is monitored at selected locations on the surface of the model. The data is transported into frequency space by using the Fast Fourier Transform function in MATLAB. The SPL can

be plotted as a function of Strouhal number, St, which is a normalized frequency defined in this study as

$$St = \frac{\omega D}{U_\infty} \tag{2.3.7}$$

where ω is frequency.

2.4 Wall Treatment

In the PANS simulation the flow field in the vicinity of the walls is treated specially with a generalized wall treatment, also known as Hybrid Wall Treatment. It was proposed by Popovac and Hanjalic [12] as a way to force a smooth change between viscous sublayer formulations and the standard wall functions for the turbulence model. In general, for this wall treatment, a flow property Φ_P at the first near-wall grid node is evaluated using a blending principle according to

$$\Phi_P = \Phi_\nu e^{-\Gamma} + \Phi_t e^{-1/\Gamma} \tag{2.4.1}$$

$$\Gamma = \frac{0.01 y^{+4}}{1 + 5y^+} \tag{2.4.2}$$

where ν and t represent viscous and fully turbulent expressions respectively.

Chapter 3

Method

In this chapter the model geometry is introduced, the wind tunnel experiment by Ventakrishnam et al. is briefly described, the boundary conditions and numerical schemes are introduced and temporal and physical resolution is reported. Finally the computational mesh is described.

3.1 Model Geometry

Figure 3.1.1 shows the computational domain (also referred to as "the wind tunnel") and the position of the RLG inside it. The length of the domain in terms of wheel diameter D is 15 D. The center of the RLG is located five diameters from the inlet and 10 diameters from the outlet. The cross section of the tunnel is a constant square with 3.69 D sides with the RLG centered in that cross section. The direction of the flow is indicated with an arrow and U_∞. Figure 3.1.2 shows the dimensions of the RLG. All the dimensions are kept the same as in the experiment by Ventakrishnam et. al [3]. The dimensions are as follows: wheel width 0.37D and wheel shoulder radius 0.115D; wheelbase 1.16D and track 0.88D; transverse axle square with side 0.3D, longitudinal beam 0.3D high and 0.25 wide; vertical post 0.25D square.
In the discussion of the results the terms "wing side" and "ground side" are used. The wing side is toward the positive y-direction (where on a real airplane the wing would be located) and the ground side is toward the negative y-direction (where the ground should normally be relative to a airplane). Another convention in the discussion that follows is that the side of the wheels which is adjacent to the truck (the truck includes the vertical post, beam and axles) is referred to as the inboard side and the opposite side is referred to as the outboard side.

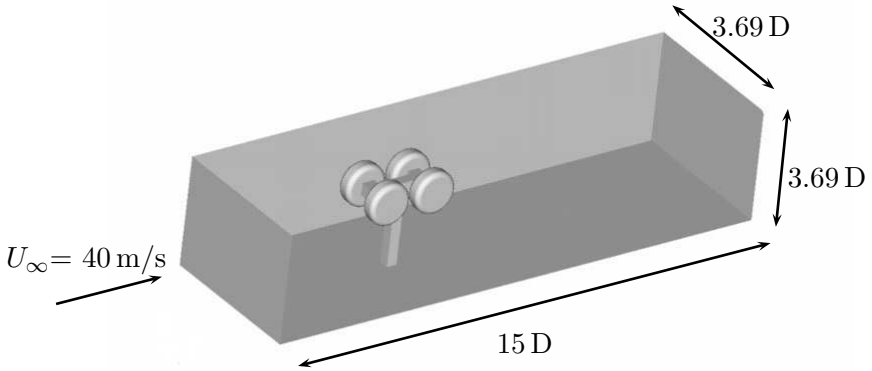

Figure 3.1.1: *The computational domain showing the RLG inside. The inlet is located 5 wheel diameters from the center of the model and the outlet 10 wheel diameters fromt it. The inlet velocity is U_∞ = 40 m/s. (Courtesy of Krajnović and Helgason [13])*

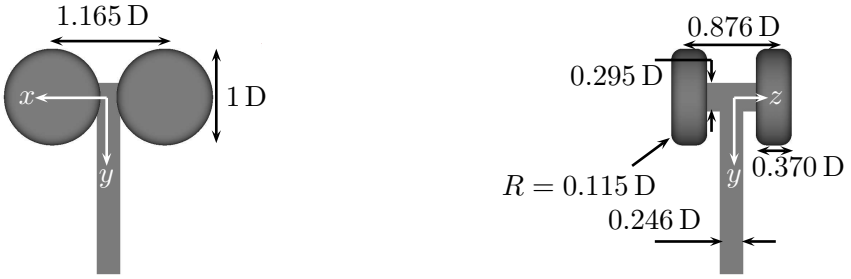

Figure 3.1.2: *Dimensions of the landing gear and the definition of the coordinate system. (Courtesy of Krajnović and Helgason [13])*

3.2 Wind Tunnel Experiments by Ventakrishnam et al.

The RLG was tested in a wind tunnel at the National Aerospace Laboratories, Bangalore, India. With the free stream velocity U_∞ = 40 m/s the Reynolds number based on the wheel diameter was $Re_D = 1 \times 10^6$. The free stream velocity was uniform within 0.2 % across the wind tunnel with turbulence level within 0.12 %.
The experimental data available consists of oil flow visualization photographs, unsteady and averaged surface pressure and forces on the entire model. Other results such as the sound pressure level (SPL) and the pressure force acting on the wheels are derived from that data.
When comparing the simulated surface flow field with the oil flow visualization from the experiment, averaged streamlines (also called particle trace lines) are used. Oil flow visualization is performed covering the model with a mixture of oleic acid, titanium dioxide powder and oil. The flow pattern then forms naturally in the wind tunnel and is allowed to reach a steady form. The model is then photographed. These photographs are compared to the surface streamlines figures from this studies simulations and should result in similar flow pattern. It should be noticed that gravitational and inertia forces are present to some extent when oil flow patterns develop whereas no such forces are considered in the simulations.
Further information about the experiment and the measurement techniques used can be found in the paper by Ventakrishnam et al. [3].

3.3 Numerical Method and Boundary Conditions

The equations presented in chapter 2 are discretized and solved on a collocated finite volume grid using the commercial solver AVL FIRE. The convective fluxes are approximated with 95% central differencing and 5% upwind differences in the LES and a second order upwind scheme in the PANS simulation. The continuity equation is discretized using pure central differences. A second-order accurate three-time level scheme was applied for time integration. Boundary conditions are as follows: uniform, constant velocity $U_\infty = 40$ m/s is set at the inlet. Homogeneous Neumann boundary condition is set at the tunnels outlet and the tunnel walls are treated as slip walls. The surface of the model has no-slip boundary condition. Non-dimensional time step is $\Delta t = 0.002 \cdot D/U_\infty$.
Table 3.3.1 shows the spatial resolution in terms of wall units and time resolution in terms of CFL number. In general, wall normal resolution under n^+=1 is considered sufficient for LES and RANS models. The requirements in the length wise and span wise directions for LES are $s^+ \leq 30$ and $l^+ \leq 100$ respectively [14]. These general requirements are met in the wall normal direction on the wheels but not on the truck. Furthermore, the span wise and length wise resolution is far from meeting these requirements on the entire model as can be read from the table. The temporal resolution in terms of CFL number can be

Table 3.3.1: *Spatial resolution. n^+ , s^+ and l^+ denote wall normal, span wise and length wise resolution in wall units, respectively.*

	wheels		**truck**	
	n^+	s^+,l^+	n^+	s^+,l^+
LES	max=7.94, ave = 0.19	$\leq$ 450	max=14.8, ave=3.28	$\approx$ 500
PANS	max=7.51, ave = 0.15	$\leq$ 400	max=16.7, ave=3.80	$\approx$ 650

summarized as follows: For the LES the maximum CFL number is 12 and the average CFL in the domain is 0.05. For the PANS the maximum CFL number is 11 and the average CFL in the domain is 0.05. Table 3.3.2 shows the run time of simulation before averaging started. It is important that the simulation has reached a fully developed conditions before averaging can begin. The table reports as well the averaging time for the two simulations.
Figures 3.3.1 and 3.3.2 show instantaneous wall normal resolution in wall units n^+ on

Table 3.3.2: *Runtime of simulations.*

	run time before averaging $[tU_\infty/D]$	averaging time $[tU_\infty/D]$
LES	57	69
PANS	30	64

the wheels for both simulations. Figures 3.3.3 and 3.3.2 show instantaneous wall normal resolution in wall units n^+ on the truck for both simulations. Note that the color scale is different from the one in figures 3.3.1 and 3.3.2.

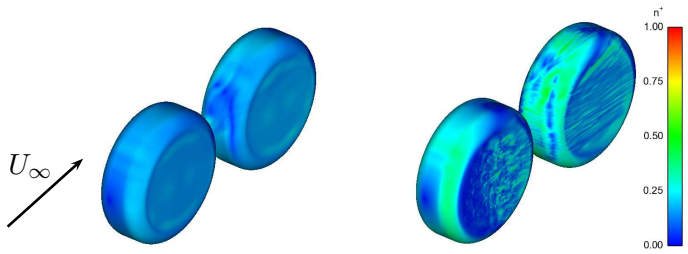

(a) PANS (b) LES

Figure 3.3.1: *Wall normal resolution in wall units n^+ on the wheels. Outboard side, view from front and above.*

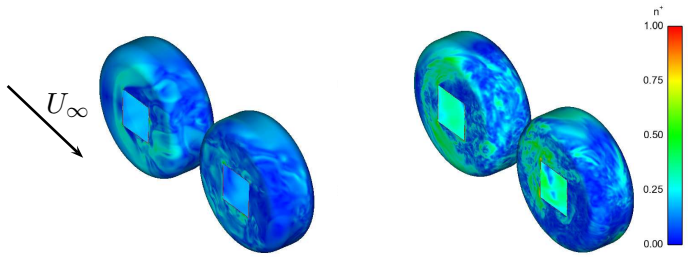

(a) PANS (b) LES

Figure 3.3.2: *Wall normal resolution in wall units n^+ on the wheels. Inboard side, view from rear and below.*

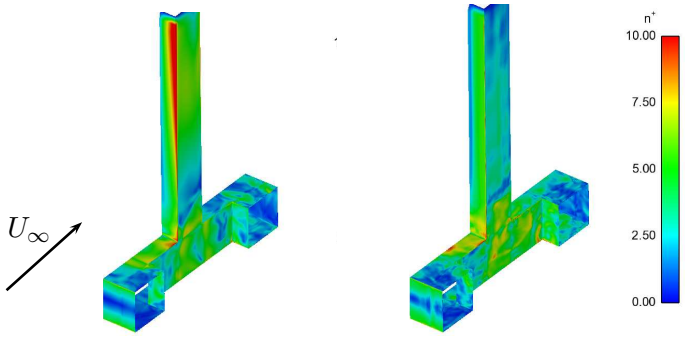

(a) PANS (b) LES

Figure 3.3.3: *Wall normal resolution in wall units n^+ on the truck. Outboard side, view from front and above.*

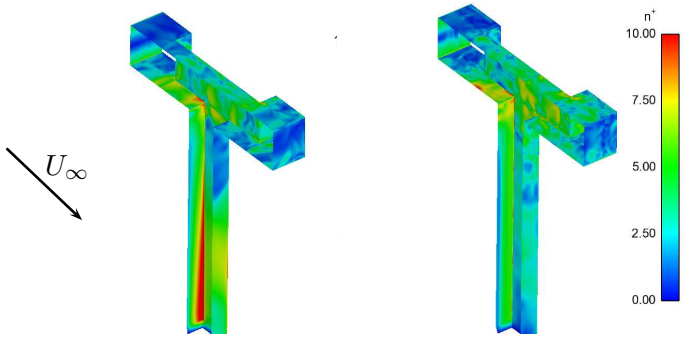

(a) PANS (b) LES

Figure 3.3.4: *Wall normal resolution in wall units n^+ on the truck. Inboard side, view from rear and below.*

3.4 Computatinal Mesh

A structured hexahedral computational mesh was created in ICEM CFD. Approximately 7 months out of 12 that were spent on the project went into the construction of the mesh. ICEM CFD uses blocking technique. The domain is manually divided into blocks and the mesh parameters (e.g. density and stretching) are defined for each block. Symmetry of the model is used and only half of the domain was meshed in ICEM, then imported to AVL FIRE and mirrored and spliced together. 1,132 blocks were used. The mesh consists of about 21 million cells. Figure 3.4.1(a) shows the blocking structure that was made covering half the domain. Figures 3.4.1(b) and 3.4.1(c) show an example of the blocking structure around the wheel.

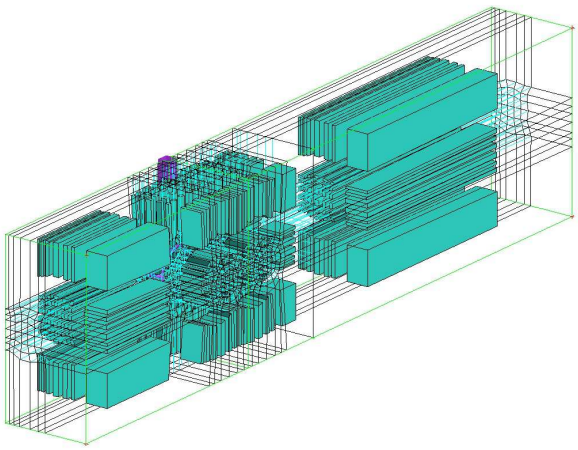

(a) *Half of the domain.*

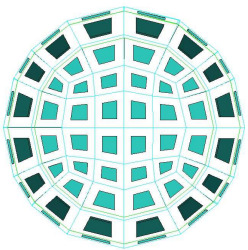

(b) *Wheel, outboard side.*

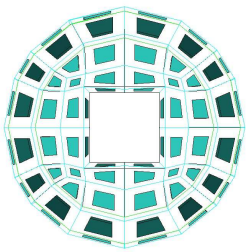

(c) *Wheel, inboard side.*

Figure 3.4.1: *Blocking structure in ICEM CFD.*

Figures 3.4.2 to 3.4.4 show the computational mesh. Most of the cells are concentrated around the wheels and the truck because there the flow is expected to be complex and highly turbulent containing a wide range of turbulent scales.

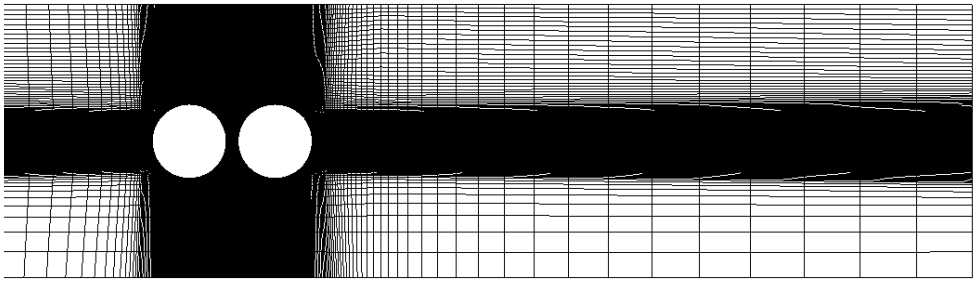

(a) *Whole domain.*

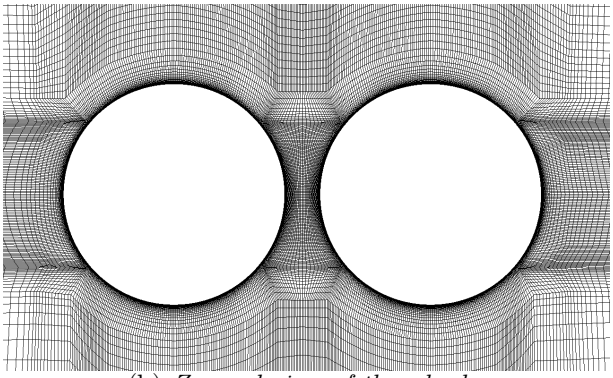

(b) *Zoomed view of the wheels.*

Figure 3.4.2: *z-cut through the volume mesh.*

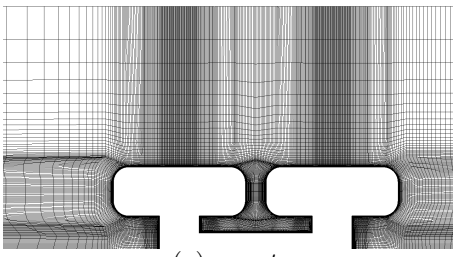

(a) *y-cut.*

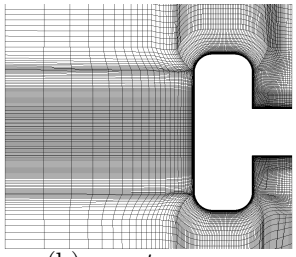

(b) *x-cut.*

Figure 3.4.3: *Cut through the volume mesh.*

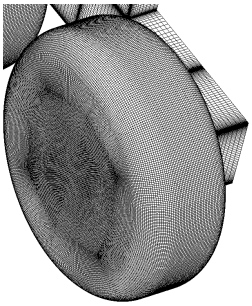

(a) *Outboard view.*

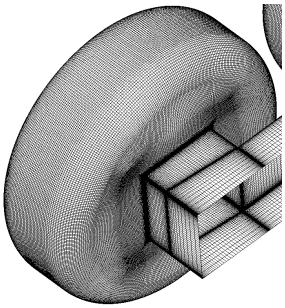

(b) *Inboard view.*

Figure 3.4.4: *Surface mesh of the landing gear.*

Chapter 4

Results

In this chapter the results of the LES and PANS simulations are presented and comparison is made with experimental data wherever possible. First the averaged surface streamlines are compared with oil flow visualization photographs. Then the streamlines in the flow field are investigated and the difference between the two simulations is discussed (no experimental data is available in the outer flow field). Averaged surface pressure is then compared to experimental data and time history of pressure at selected monitoring locations is investigated and compared to experimental data. The filter resolution in the PANS simulation is investigated in order to cast a light on how much is resolved. Lastly the forces acting on the model and pressure forces acting on the wheels are compared with experimental values.

4.1 Streamlines

Streamlines produced from the time averaged velocity field in the simulations and the oil flow visualization from the experiment are compared in figures 4.1.1 to 4.1.6.
Figure 4.1.1(c) shows a false separation at the leading outboard edge of the front wheel in the LES results. This separation is not present in the experimental results, figure 4.1.1(a) or in the PANS simulation, figure 4.1.1(c). The impingement lines on the front of the rear wheel are well predicted by both simulations. On the outboard side of the rear wheel in the LES results the flow is bent a bit too much to the wing side and ground side. Especially the flow bends toward the wing side and forms wavy flow pattern which is not visible in the experimental results. The PANS results however shows a good prediction on this side. There the flow is slightly bent toward the wing side and that is in agreement with the experimental results (perhaps not clear in the figure but closer examination of the photographs reveals this).
Figure 4.1.2 shows the ground side of the landing gear. The streamlines in the PANS on the bottom of the front wheel, figure 4.1.2(b), agree well with the experimental figure (4.1.2(a)). The LES fails (figure 4.1.2(c)) predicting a focus and accompanying bifurcation lines and a saddle where there should be attached flow. The bottom of the rear wheel is also in fair agreement with the experimental results for PANS and the LES is not far off either. In the rear outboard corner of the rear wheel in the figure the PANS performs slightly better in predicting the shape of the streamlines. Under the front axle the oil flow figure does not reveal much as this region is immersed in a separation bubble where the velocity is low. The simulations show a saddle in that region of different sizes and locations. Both simulations are in fair agreement with the experimental results under the rear axle with a focus on the corner of the beam and axle. Figure 4.1.3 shows the intersection of the longitudinal beam and the vertical post. The general flow pattern is replicated well by both LES and PANS simulations and LES seems even to be performing better between

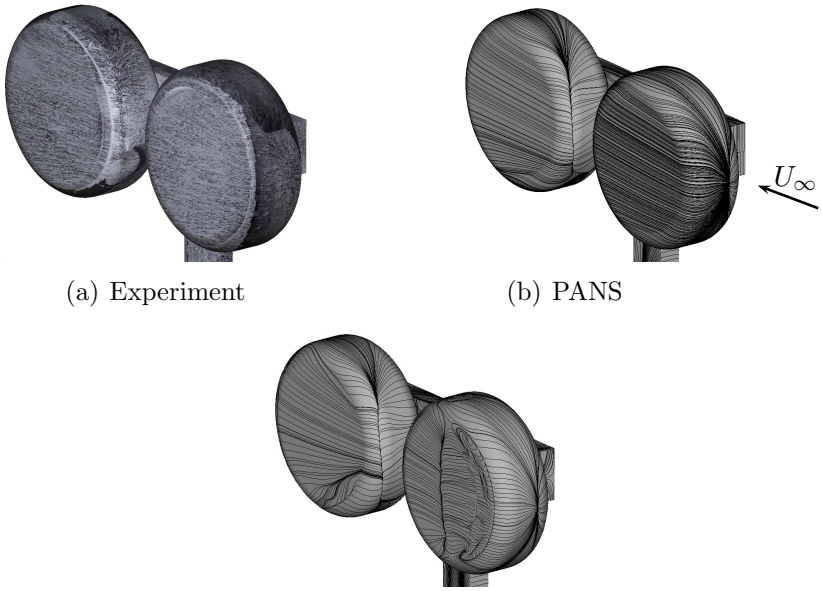

(a) Experiment (b) PANS

(c) LES

Figure 4.1.1: *Streamlines. Outboard view from front.*

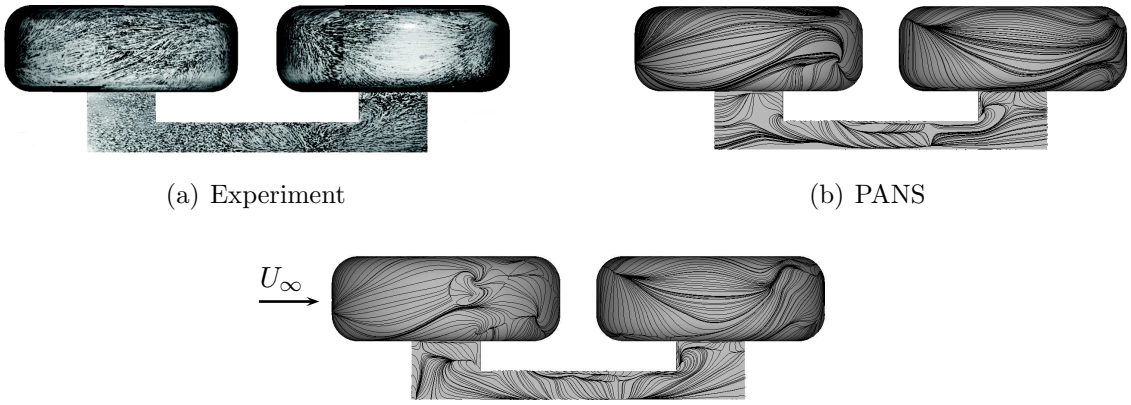

(a) Experiment (b) PANS

(c) LES

Figure 4.1.2: *Streamlines, looking up from under the wing side.*

the front axle and the beam-post intersection. Figure 4.1.4 shows the inboard side of the wheels. The streamlines on the front wheel capture the flow pattern in the experimental results rather well for both simulations. There exists small differences between the LES and PANS especially at the location marked with R. For the upstream side of the rear wheel the two simulations agree with the experimental results on the wing side however there are bifurcation lines close to the wheel shoulder on the ground side in the experimental results that are captured by the PANS simulation but not LES. Downstream of the truck exists a dead air region seen by lack of trace lines in the oil flow. Here the two simulations show different flow patterns. Figure 4.1.5 shows the rear and outboard side of the front wheel. The separation on the outboard side in the LES has already been discussed. Here the early separation along the circumference in the LES is also visible. On the rear side there is a large focus (marked in the figure) which is present in both simulations and in the experimental results. Notice also that the bifurcation lines marked with B in figure 4.1.5(c) are also captured in both simulations. Figure 4.1.6 shows the rear and outboard sides of the rear wheel. The trace lines along the outboard side of the wheels are more uniform and

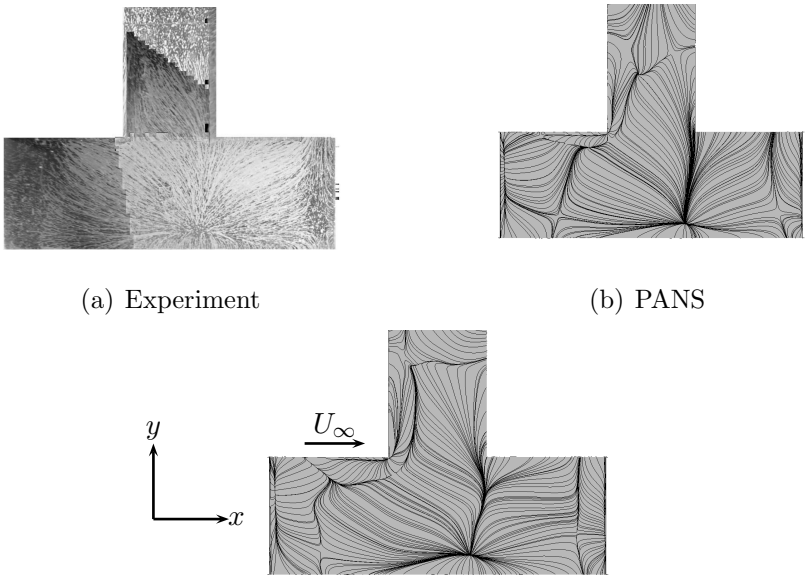

(a) Experiment (b) PANS

(c) LES

Figure 4.1.3: *Oil flow visualization and streamlines. Side view of truck.*

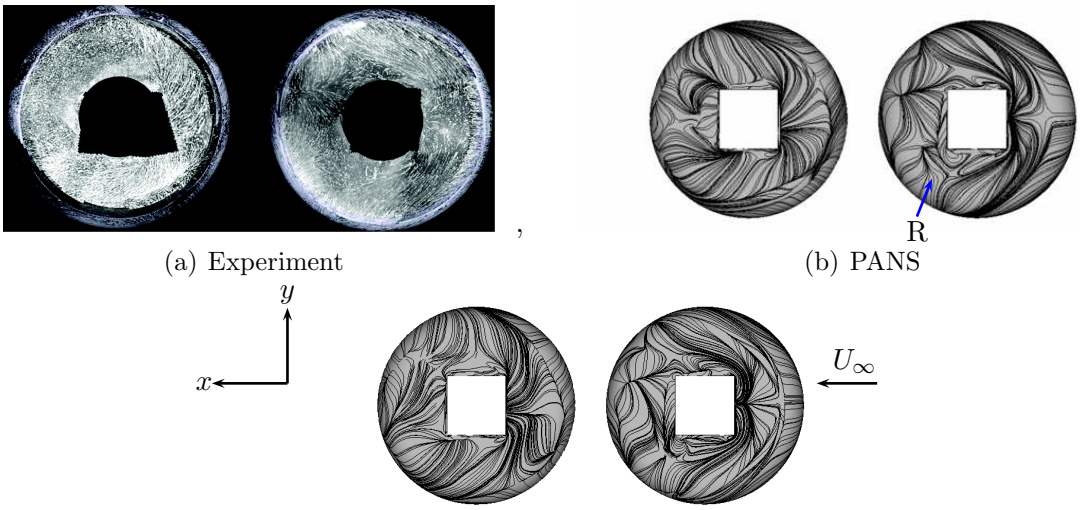

(a) Experiment (b) PANS

(c) LES

Figure 4.1.4: *Oil flow visualization and streamlines, inboard view of wheels.*

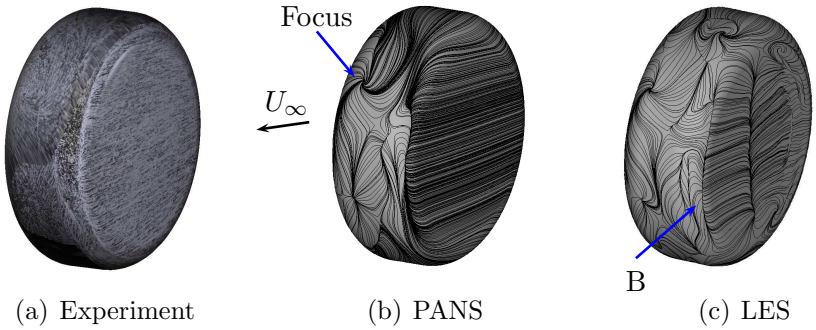

(a) Experiment (b) PANS (c) LES

Figure 4.1.5: *Oil flow visualization and streamlines on front wheel, view from rear.*

straight for the PANS simulations and in good agreement with the experimental results whereas in the LES the streamlines are bent toward the shoulders and near the wing side

shoulder the lines become distorted. On the rear side the two simulations show different patterns both not in good agreement with the experimental results. In the PANS results the flow remains attached longer over the circumferential than in the LES and that agrees better with the experimental results. Figure 4.1.6 shows the streamlines projected onto

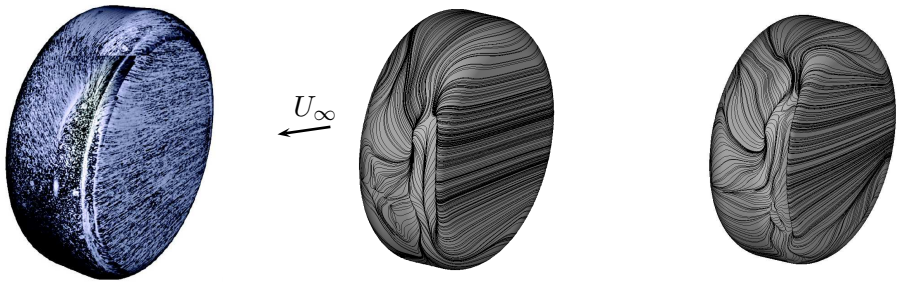

(a) Experiment (b) PANS (c) LES

Figure 4.1.6: *Oil flow visualization and streamlines on rear wheel, view from back.*

the x - z plane going through the center of the wheels ($y = 0$) for both simulations. The plane is colored with pressure. It shows a clear difference in the flow field between the simulations. The artificial separation bubbles on the outboard sides of the front wheels in the LES is visible. The form of the trailing wake is also very different between the two simulations. The fair amount of symmetry of these time averaged streamlines suggest that simulation times are sufficient. However the flow field is not completely symmetric due to possible fluctuations in the flow that have low frequencies that the averaging time did not capture. Figure 4.1.8 show the streamlines projected on to the x - y plane colored with

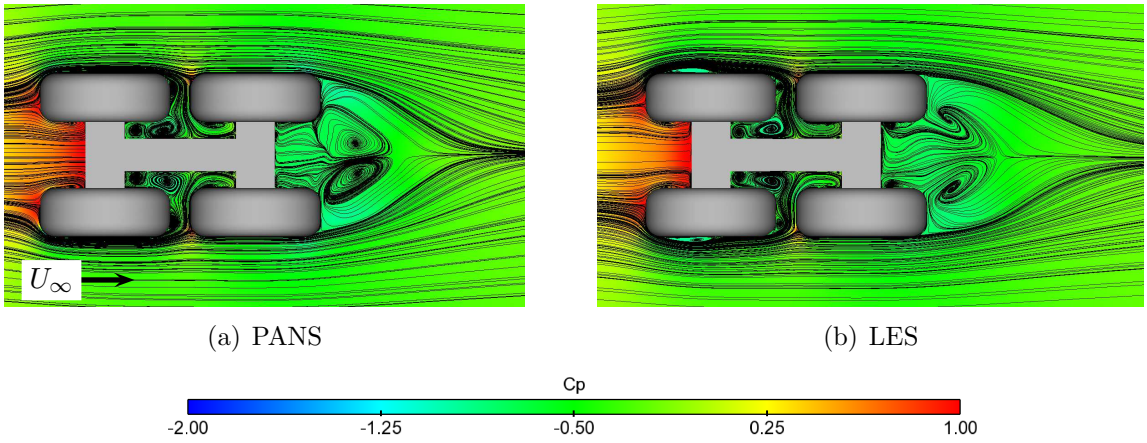

(a) PANS (b) LES

Figure 4.1.7: *Streamlines projected onto the plane going through the center of the wheels.*

pressure going through various z values. Overall, the flow fields are quite different between simulations.
In figures 4.1.8(a) and 4.1.8(b) it can be seen that the number of vortexes are the same for both simulations but differ in shape and position.
Figures 4.1.8(c) and 4.1.8(d) shows further differences in the flow. Especially the big vortex above the rear axle in the PANS simulation has a definite and strong recirculation whereas the LES shows the same vortex with less recirculation. Also, the PANS simulation shows two vortex cores behind the rear axle, one small behind the wing side corner and another bigger behind the smaller one. The LES does not show this smaller vortex. Figures 4.1.8(e) and 4.1.8(f) show where the flow is attached over the circumference and where it reattaches.
Figure 4.1.9 shows the streamlines projected on the z - y plane colored with pressure going

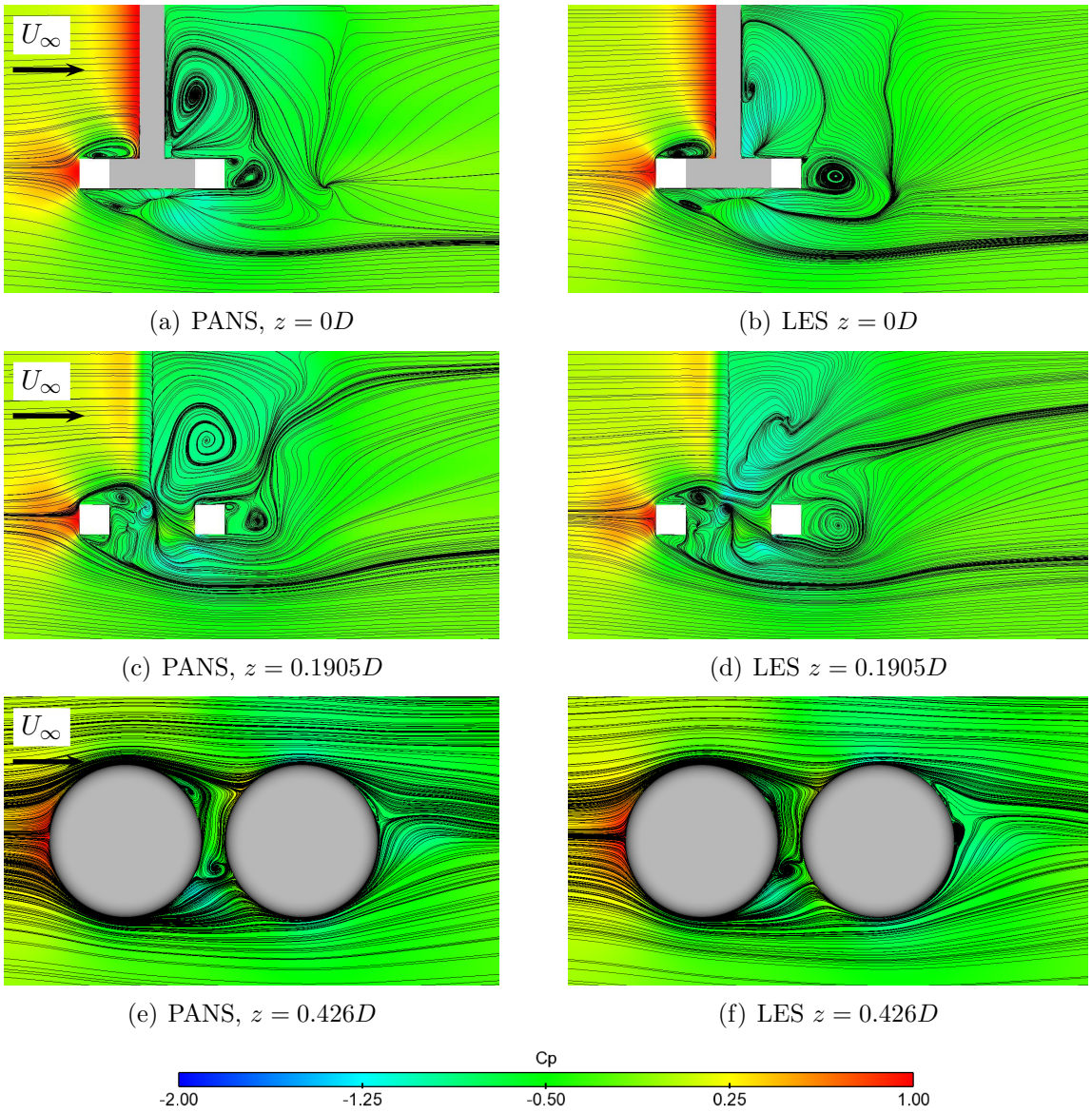

(a) PANS, $z = 0D$ (b) LES $z = 0D$

(c) PANS, $z = 0.1905D$ (d) LES $z = 0.1905D$

(e) PANS, $z = 0.426D$ (f) LES $z = 0.426D$

Figure 4.1.8: *Streamlines projected onto plane going through several z locations.*

through various x values. For x = 0D ,figures 4.1.9(a) and 4.1.9(b), show very similar stream line pattern for the simulations. However the development further downstream ,figures 4.1.9(c) to 4.1.9(h), is very different between the simulations.

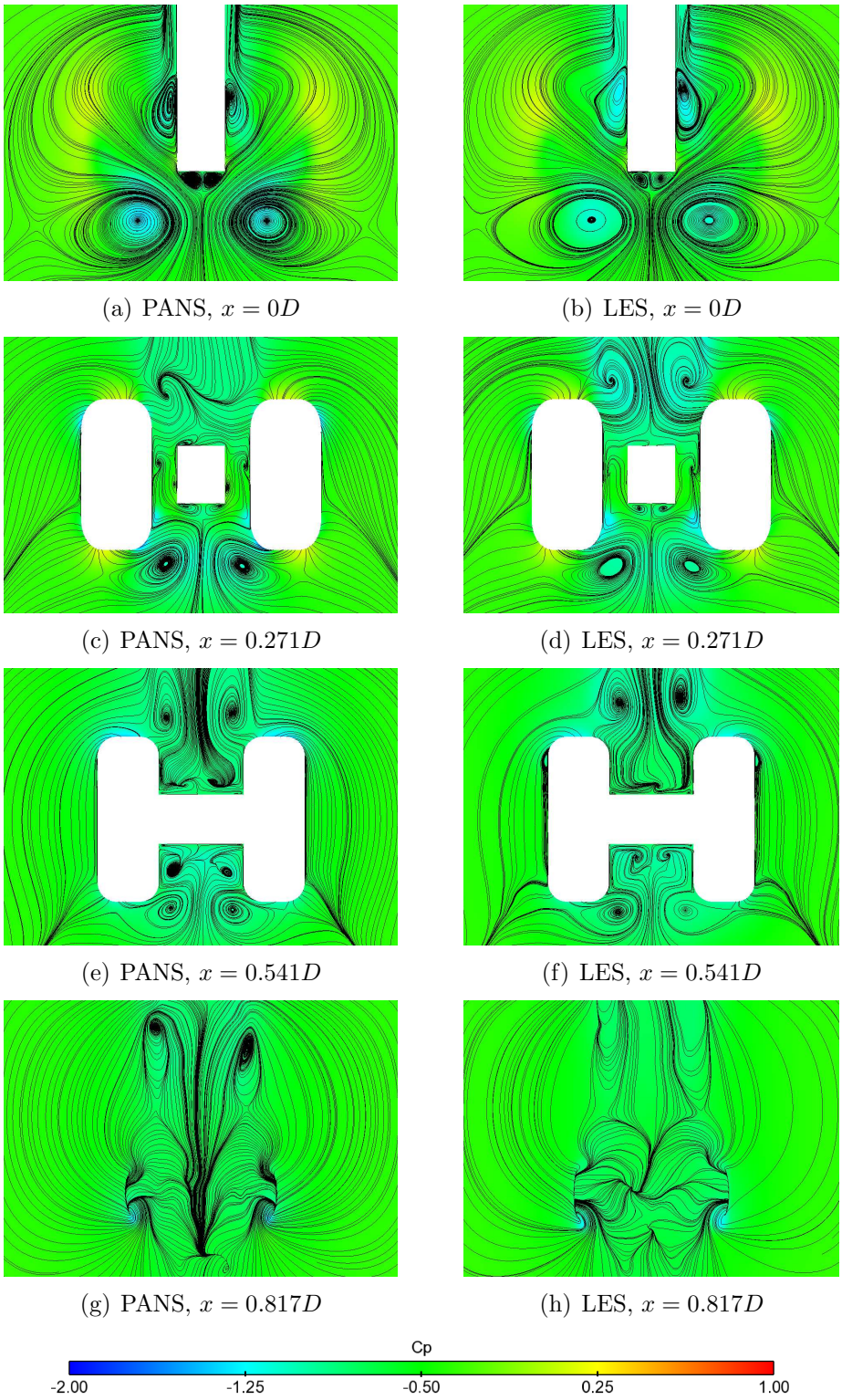

(a) PANS, $x = 0D$ (b) LES, $x = 0D$

(c) PANS, $x = 0.271D$ (d) LES, $x = 0.271D$

(e) PANS, $x = 0.541D$ (f) LES, $x = 0.541D$

(g) PANS, $x = 0.817D$ (h) LES, $x = 0.817D$

Figure 4.1.9: *Streamlines projected onto plane going through several x locations.*

4.2 Averaged Pressure

Figures 4.2.1 and 4.2.2 show pressure on the surface of the wheels. The pressure on the outboard side of the front wheel in the LES results, figure 4.2.1(b), is in poor agreement with the experimental results, figure 4.2.1(a), due to the artificial separation in the LES. The low pressure regions on the top of the rear wheel is also not well captured in the LES results whereas the PANS, figure 4.2.1(c), succeeds better there in comparison with the

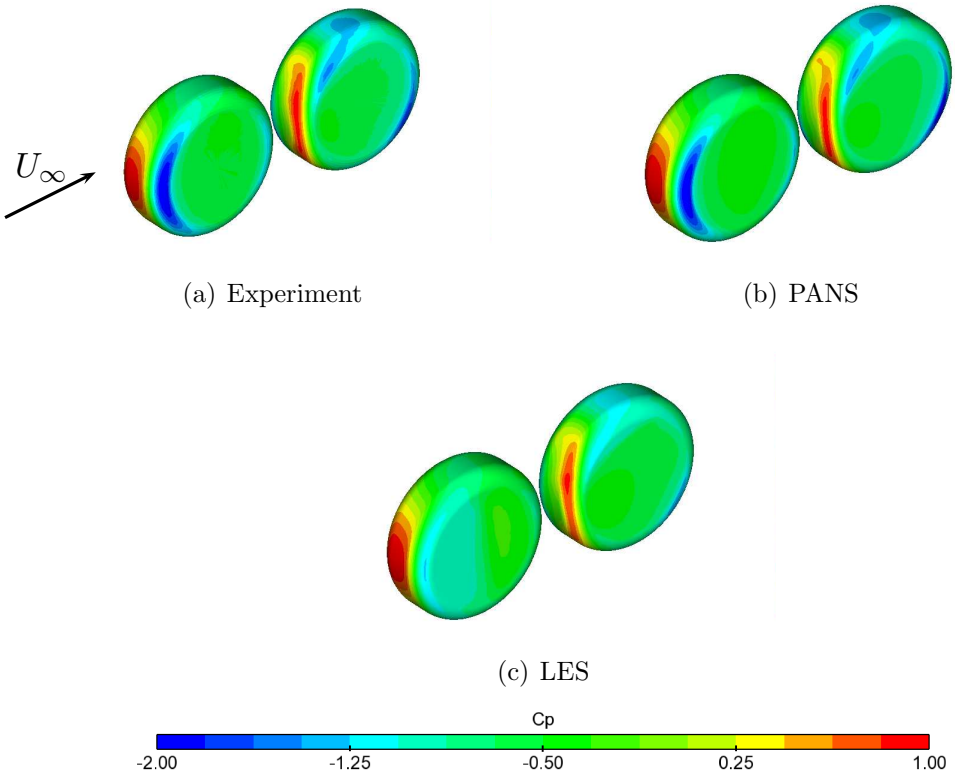

(a) Experiment (b) PANS

(c) LES

Figure 4.2.1: *C_p on the wheels. Outboard view.*

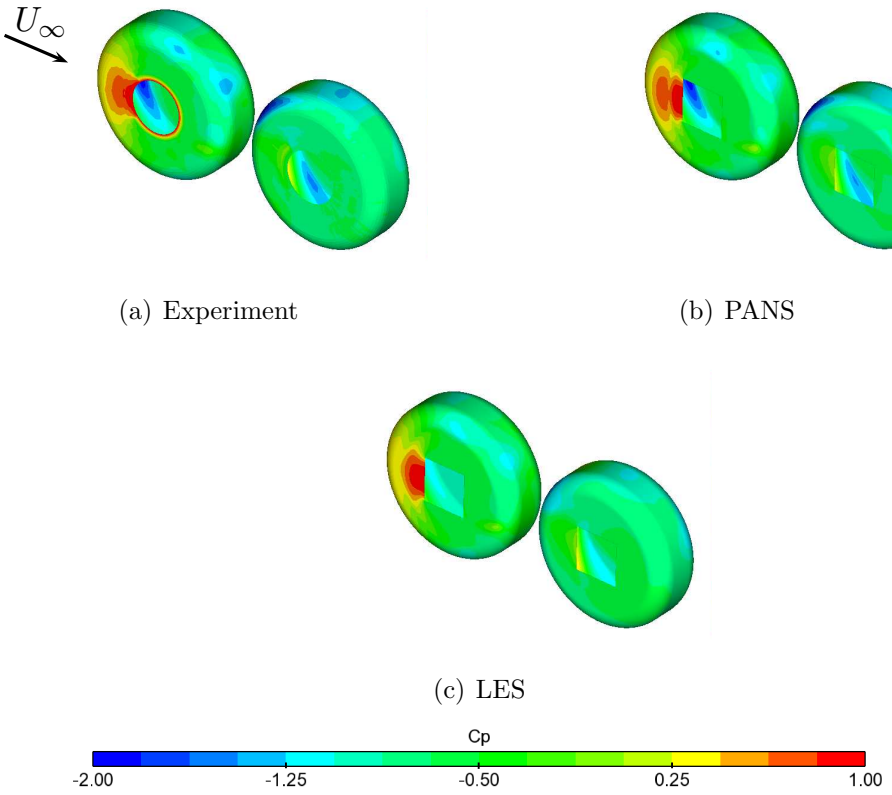

(a) Experiment (b) PANS

(c) LES

Figure 4.2.2: *C_p on the wheels. Inboard view.*

experimental results. The high pressure zone on the inboard side of the front wheel ,figure 4.2.2, just ahead of the front axle is badly represented by both simulations, especially in the PANS simulation, figure 4.2.2(c). Figures 4.2.4 and 4.2.5 show pressure plotted along

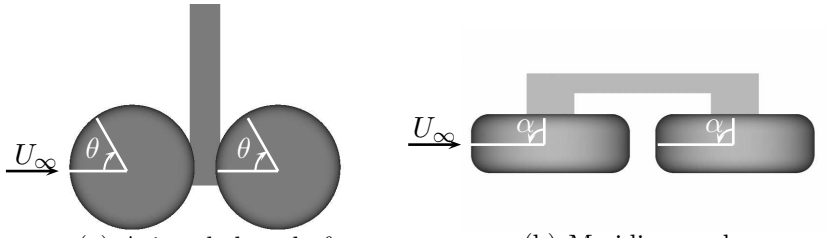

(a) Azimuthal angle θ (b) Meridian angle α

Figure 4.2.3: *Definition of θ and α angles.*

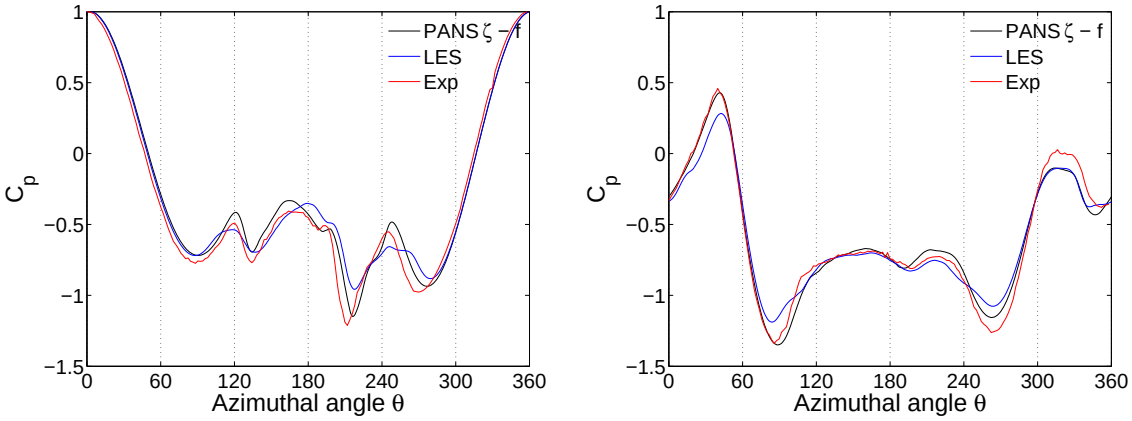

(a) Front wheel (b) Rear wheel

Figure 4.2.4: *C_p along the circumference of wheels, $z = 0.4263D$.*

the meridians and center azimuthal of the wheels. For definitions of the angles θ and α see figure 4.2.3. From looking at these plots it can be concluded that PANS predicts the pressure better than LES. Notice in figure 4.2.5(a) the LES results from $\alpha = 120°$ to $\alpha = 240°$ where the influence from the artificial separation is evident. It seems as the PANS performs better along the meridian lines than the azimuthal. This could be caused by difficulty in predicting separation along the circumference of the wheel.

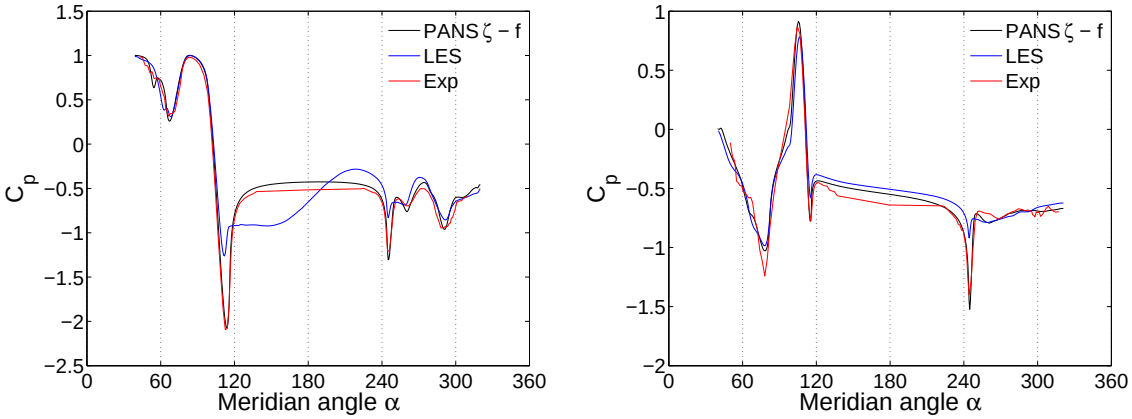

(a) Front wheel (b) Rear wheel

Figure 4.2.5: *C_p along the meridian plane of wheels, $y = 0D$.*

4.3 Sound Pressure Level (SPL)

Figure 4.3.1 shows the sound pressure level (SPL) on the outboard side of the wheels. The color scale in the experimental figure could not be reproduced for our simulations results and therefore it can cause difficulties when comparing the results. The SPL on the outboard side of the front wheel is significantly higher in the LES results compared with the PANS results. The reason is the artificial separation in the LES results which causes greater pressure fluctuations in the separation bubble than in the attached flow of the PANS results. Figure 4.3.2 shows the SPL on the inboard side of the wheels for the

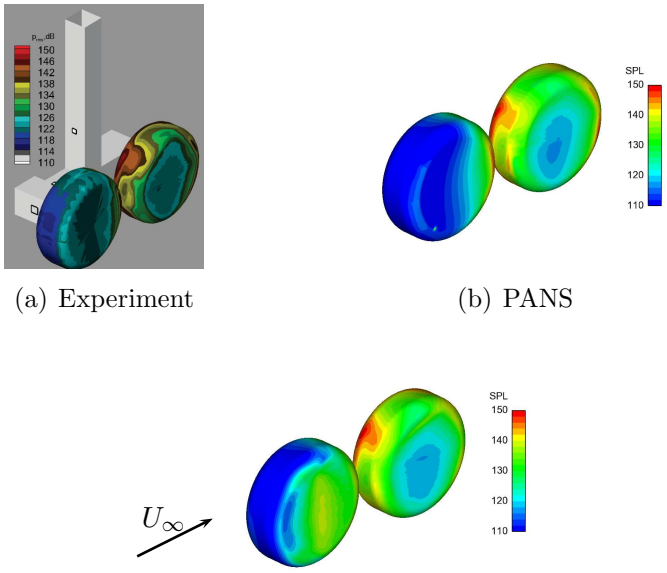

(a) Experiment (b) PANS

(c) LES

Figure 4.3.1: *SPL on the wheels. Outboard view.*

two simulations. No experimental data was available for the SPL on the inboard side of the wheels at the time of writing this report. Notice higher SPL on the upstream part of the rear wheel and the rear side of the front wheel in the PANS simulation.

The time history of the pressure at selected locations on the models surface was sampled

(a) PANS (b) LES

Figure 4.3.2: *SPL on the wheels. Inboard view.*

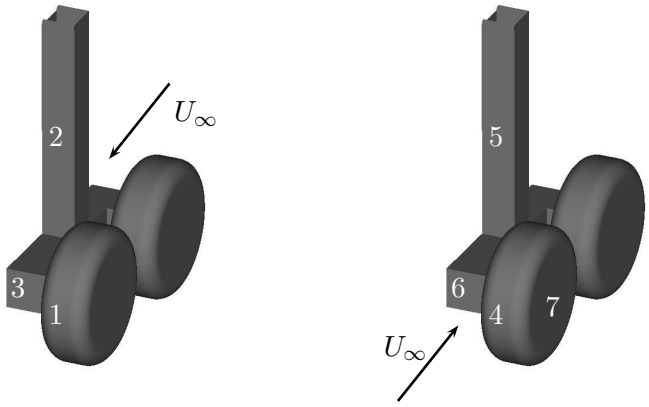

(a) *Spectra sampling points rear.* (b) *Spectra sampling points front.*

Figure 4.3.3: *Locations of sampling points reported in figures 4.3.4 and 4.3.5.*

and the resulting sound pressure level reported in figures 4.3.4 and 4.3.5 where the SPL is plotted against Strouhal number. The locations of these points are shown in figure 4.3.3. Point 1, figure 4.3.4(a), is on the back of the rear wheel, immersed in the wake of the model. The simulations share the general shape of the experimental curve however report higher SPL than the experiment with PANS proving to have higher SPL than LES. Point 2, figure 4.3.4(b), is on the back of the vertical post. For the high Strouhal numbers, the simulations and the experimental results exhibit a linear trend. This linear trend exists further into the low Strouhal number range for the PANS simulation than the LES. Notice how the narrow range of SPL for the high Strouhal numbers for the simulations is in contrast with the wider range in the experimental results. A direct comparison of the range of SPL for a given Strouhal number should be avoided because the sampling time for the experiment is significantly longer than in the simulations and is the reason for that the experimental data exists for much lower Strouhal numbers than in the simulation data. Point 3, figure 4.3.4(c), is at the back of the rear axle. The simulation results fall within a reasonable range of SPL compared with the experimental results for the high Strouhal numbers but over predict for Strouhal numbers lower than ten. In contrast there is no such over prediction for the low Strouhal numbers at point 4 in figure 4.3.4(d), located at the front of the front wheel. Notice the peak in the LES results at about St = 1. Also noteworthy is the fact that for the St = 500 to St = 10,000 the simulations do not exhibit higher SPL than 60 whereas the experiment shows that much of the data for that Strouhal number range is above SPL = 60. The behavior of the SPL in point 5, figure 4.3.5(a), located on the front side of the vertical post and point 6, figure 4.3.5(b), which is located on the front side of the front axle is similar to that of point 4.

Point 7, figure 4.3.5(c), is located at the center of the outboard side of the front wheel. For the PANS simulation and the experimental results the flow is attached over the outboard side of the front wheel and there the behavior is similar to points 4 to 6. The LES exhibits much higher SPL than the PANS and the experimental results at point 7 because of the artificial separations at the front wheel. This is in agreement with figure 4.3.1(b).

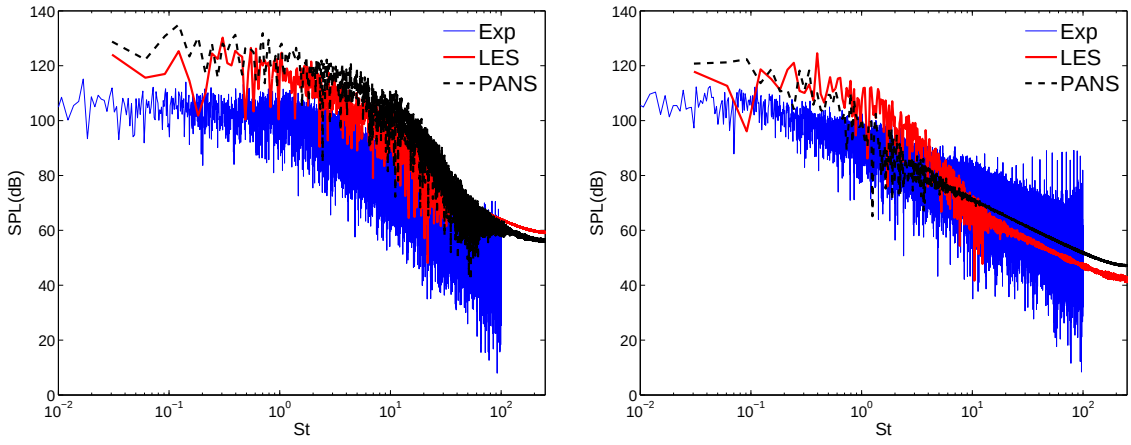

(a) Point 1 (b) Point 2

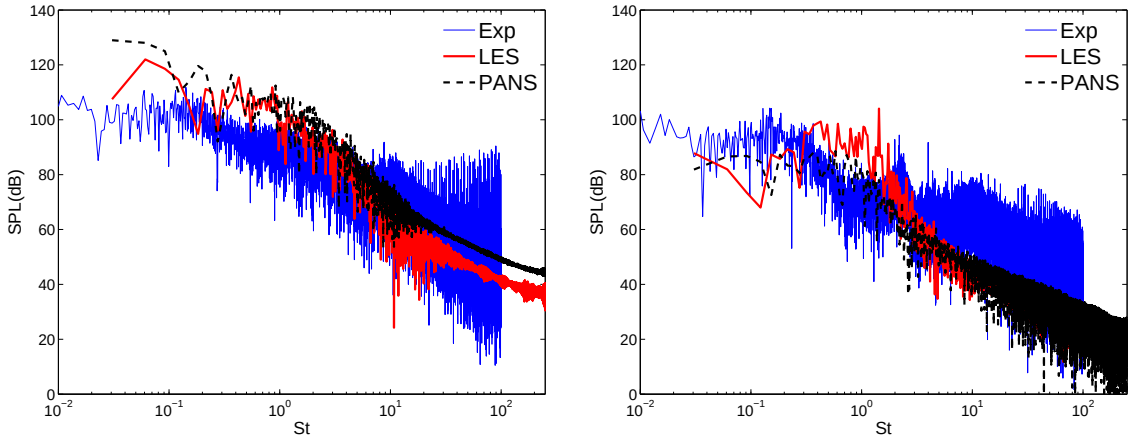

(c) Point 3 (d) Point 4

Figure 4.3.4: *SPL in points 1 to 4 on the surface of RLG in Fig. 23.*

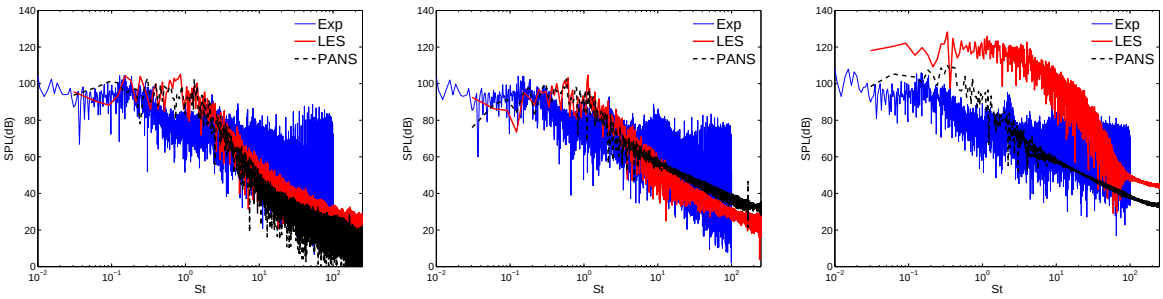

(a) Point 5 (b) Point 6 (c) Point 7

Figure 4.3.5: *SPL in points 4 to 7 on the surface of RLG in Fig. 23.*

4.4 PANS Filtering

The filtering parameter f_k is defined in equation 2.1.20. Value of $f_k = 1$ suggests maximum filtering and the equations solved reduce to pure RANS equations. Value of $f_k = 0$ suggest minimum filtering. However, this filtering parameter does not explicitly control how much is resolved and how much is filtered. This parameter is computed according to equation 2.1.20 at the end of each time step and then inserted as a constant into the RANS equations (see section 2.1). The entire set of the flow equations and RANS equations are solved in the next time step and the filtering parameter updated. Figure 4.4.1 compares the filter parameter f_k and the computed ratio $f_{k,comp} = k_u/k$. When this ratio reaches zero, it suggests that all turbulent kinetic energy is resolved. From these figures it can be seen that inboard of the wheels much is resolved and even more is resolved in the wake of the wheels. A little less is resolved in the wake of the vertical post.

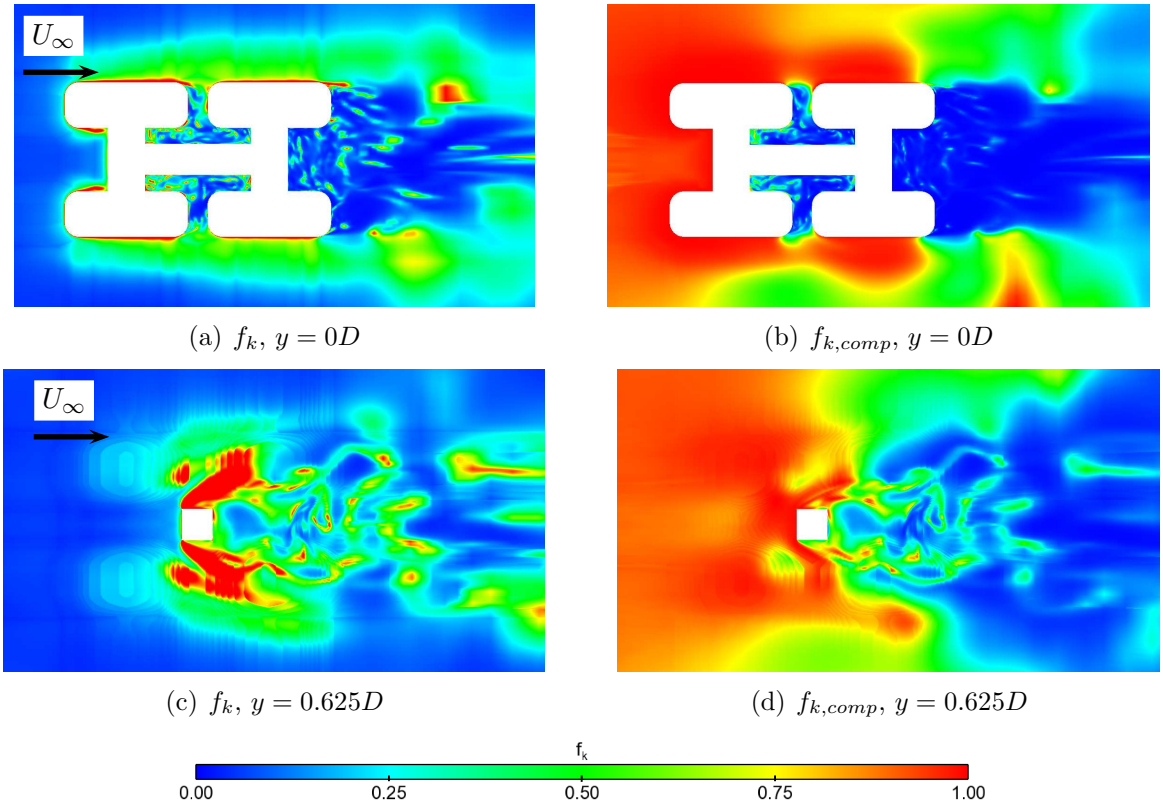

(a) f_k, $y = 0D$ (b) $f_{k,comp}$, $y = 0D$

(c) f_k, $y = 0.625D$ (d) $f_{k,comp}$, $y = 0.625D$

Figure 4.4.1: *Comparison of the filtering parameter f_k (left column) and the computed ratio $f_{k,comp}$ (right column) for the PANS simulation in the x - z plane for two different y locations. (the color scale applies to both quantities).*

It can be interesting to look at the turbulent viscosity ν_u and the dissipation ε shown in figure 4.4.2. The turbulent viscosity has been normalized with the laminar viscosity, ν. Notice that the color bar in the figure is logarithmic. From figures 4.4.1 and 4.4.2 it seems that high turbulent viscosity is not highly correlated with high level of filtering. The dissipation ε, which all is unresolved, and the computed ratio $f_{k,comp}$ are highly correlated with the filtering. The reason for the value of one for $f_{k,comp}$ upstream of the model is that the flow field is undisturbed and there simply exists no resolved turbulence.

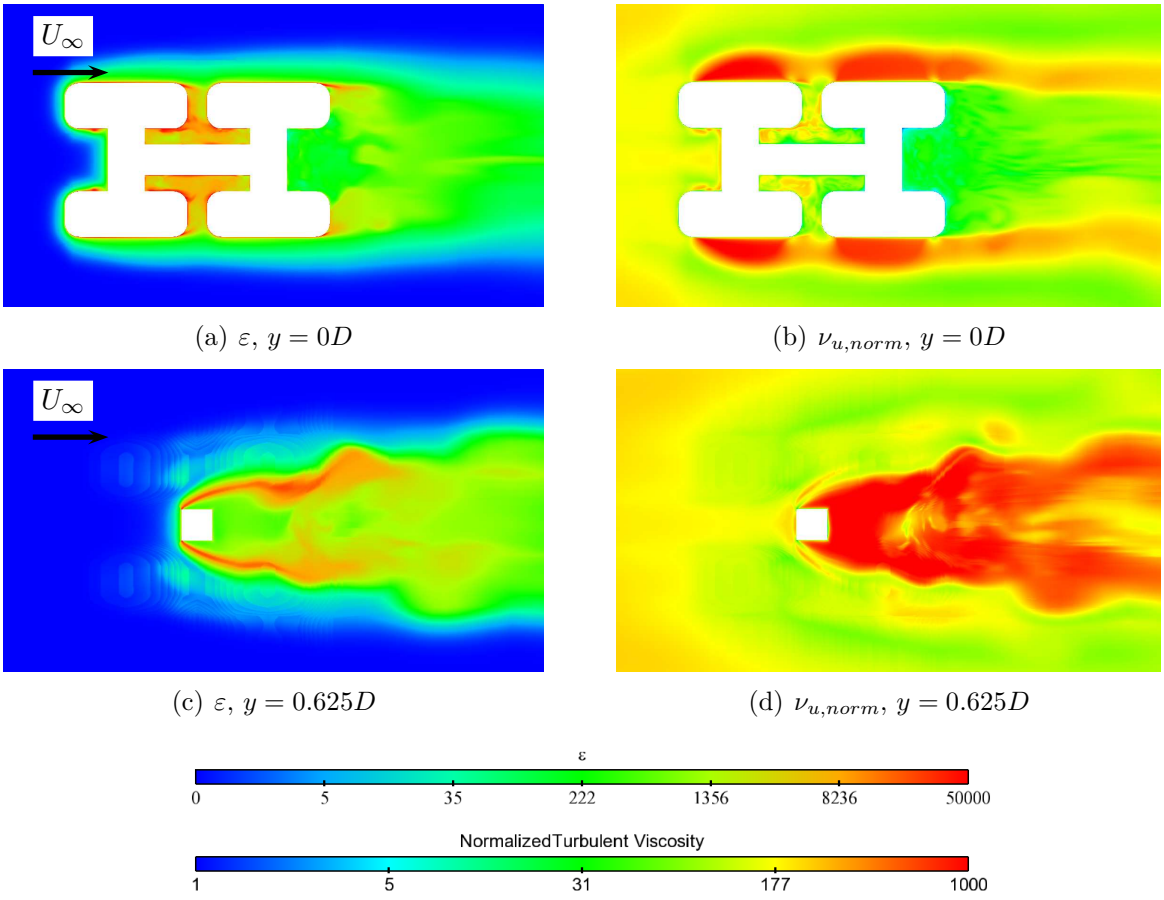

(a) ε, $y = 0D$ (b) $\nu_{u,norm}$, $y = 0D$

(c) ε, $y = 0.625D$ (d) $\nu_{u,norm}$, $y = 0.625D$

Figure 4.4.2: *Dissipation ε (left column) and the normalized turbulent viscosity, $\nu_{u,norm}$ (right column) for the PANS simulation in the x - z plane for two different y locations.*

4.5 Forces

Table 4.5.1 shows the total drag and lift force coefficients C_d and C_l respectively for the landing gear. LES drag force is 16 % higher than the drag forces measured in the experiment while the PANS drag force is 13 % higher. Notice also the higher standard deviation of drag, C_d', in the simulations than in the experiment. Interestingly, the PANS has the highest C_d'.
The lift is negative in all cases implying a net down force acting on the model. This down force is under predicted by a staggering 69 % in the LES and 66 % in the PANS simulation. For the standard deviation of lift, C_l', the simulations report over ten times higher standard deviation than in the experiment.

Table 4.5.1: *Forces on the entire model.*

	Exp	LES	PANS
C_d	1.54	1.79	1.74
C_d'	0.012	0.032	0.053
C_l	-0.62	-0.19	-0.21
C_l'	0.005	0.051	0.068

Table 4.5.2 shows the drag and lift forces resulting from pressure distribution on the surfaces, excluding the viscous drag on the wheels, with C_{dp} the pressure drag coefficient and C_{lp} the pressure lift coefficient. The simulations agree much better with the experimental

values here than for the total forces in table 4.5.1. The time history of the drag coefficient,

Table 4.5.2: *Forces on wheels computed from averaged pressure data.*

	Front wheel		**Rear wheel**	
	C_{dp}	C_{lp}	C_{dp}	C_{lp}
Exp	0.256	-0.053	0.181	-0.032
LES	0.248	-0.047	0.172	-0.013
PANS	0.225	-0.064	0.181	-0.014

C_d, and the lift coefficient, C_l, acting on the whole model for the two simulations is shown in figure 4.5.1. The coefficients are plotted against a dimensionless time unit tU_∞/D. The time scales in the force fluctuations are similar between simulations but the amplitude of the fluctuations is greater in the PANS simulation, as the standard deviation reported in table 4.5.1 suggests.

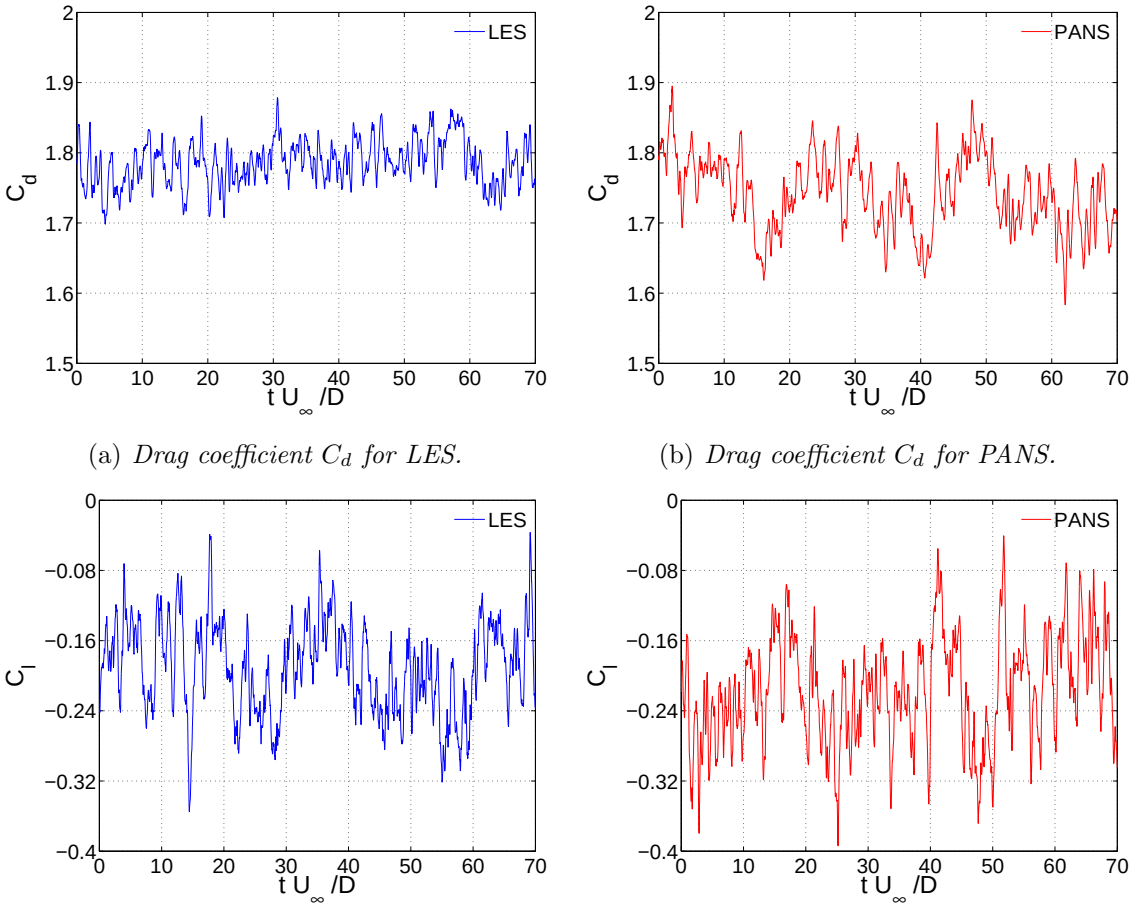

(a) *Drag coefficient C_d for LES.*

(b) *Drag coefficient C_d for PANS.*

(c) *Lift coefficient C_l for LES.*

(d) *Lift coefficient C_l for PANS.*

Figure 4.5.1: *Time history of the drag coefficient, C_d, and the lift coefficient, C_l, acting on the whole model.*

Chapter 5

Conclusions and Discussion

Based on the comparison of the simulated averaged surface streamline patterns and pressure distribution with the experimental data, which include oil flow visualization photographs and pressure port measurements, it can be concluded that PANS gives better results than LES for the particular mesh used in this study. This conclusion is strongly supported by the fact that LES produces artificial separation on the outboard side of the front wheels (see figure 4.1.1). The reason for the artificial separation is insufficient grid resolution in the LES causing it to not generate important near wall structures. It must be kept in mind that in certain areas, LES predicted averaged stream line patterns better than PANS (see figure 4.1.3). Furthermore, the comparison of averaged pressure in the plots in figures 4.2.4 and 4.2.5 suggests an overall better performance of PANS. The PANS results, being more accurate than LES, are nevertheless not extremely accurate, considering the sound pressure level (see figures 4.3.1 to 4.3.5) and pressure (see figures 4.2.4 and 4.2.5). Drawing conclusions from comparing the total forces (table 4.5.1) should be done with caution. All the simulations reported in Spalart and Mejia [2] have the drag coefficient within the range of 1.70 to 1.81 and for the lift coefficient from -0.23 to -0.18 which is comparable with this study's results. It is unclear if the simulation predictions are inaccurate or if there is error in the experimental measurement of the total forces acting on the landing gear. For the simulations the pressure forces acting on the wheels agree better with experimental values than the total forces. The total forces are measured with a force balance in the experiment whereas the pressure forces are acquired from the pressure data measured with static pressure ports on the wheels [3]. This fact rises suspicion of error in the total force measurements in the experiment.

5.1 Future work

As mentioned in the introduction, under section 1.2 , no grid dependence study has been reported. Simulations on a coarser mesh of approximately 11 million cells are underway at the time of writing this. These simulations include PANS using ζ - f turbulence model and also PANS using k - ε turbulence model as was used in the work by Girimaji [9] along with LES for reference.

Bibliography

[1] Proceedings (CDROM) of the AIAA-NASA Workshop on Benchmark Problems for Airframe Noise Computations-I (BANC-1). Stockholm, Sweden, June 0-11, 2010.

[2] P. R. Spalart and K. M. Mejia. *Analysis of Experimental and Numerical Stidies of the Rudimentary Landing Gear*. AIAA Paper, AIAA-2011-0355.

[3] L. Ventkatakrishnam, N. Karthikeyan and K. Meija. *Experimental Studies on a Rudimentary Four Wheel Landing Gear*. AIAA Paper, AIAA-2011-354.

[4] P.R. Spalart et al. *Inital noise predictions for rudimentary landing gear*, Journal of Sound and Vibration (2011), doi:10.1016/j.jsv.2011.03.012

[5] Barry S. Lazos. *Mean Flow Features Around the Inline Wheels of Four-Wheel Landing Gear*, AIAA Journal, Vol. 40, No. 2, 2002, pp. 193-198.

[6] S. Girimaji, R. Srinivasan, and E. Jeong. *PANS Turbulence Models for Seamless Transition Between RANS and LES: Fixed Point Analysis and Preliminary Results*. ASME paper FEDSM2003-45336.

[7] B. Basara, S. Krajnovic and S. Girimaji. *PANS methodology applied to elliptic-relaxation based eddy viscosity transport model*. Turbulence and Interactions Notes on Numerical Fluid Mechanics and Multidisciplinary Design, 2010, Volume 110/2010, 63-69, DOI.

[8] S. Krajnović and L. Davidson. *Large Eddy Simulation of the Flow Around a Three-Dimensional Bluff Body*. AIAA paper, AIAA-2001-0432.

[9] S. Girimaji. *Partially-Averaged Navier-Stokes Model for Turbulence: A Reynolds-Averaged Navier-Stokes to Direct Numerical Simulation Bridging Method*, ASME Journal of Applied Mechanics, Vol. 74, MAY 2006, pp. 413-421.

[10] K. Hanjalić, M. Popovac and M. Hadžiabdić. *A robust near-wall elliptic-relaxation eddy-viscosity turbulence model for CFD*. International Journal of Heat and Fluid Flow, Vol. 25, 2004, pp. 1047-1051.

[11] P. Durbin. *Near-Wall Turbulence Closure Modeling Without "Damping Functions"*, Theoret. Comput. Fluid Dynamics, Vol. 3. 1991, pp. 1-13.

[12] M. Popovac and K. Hanjalić. *Compound Wall Treatment for RANS Computation of Complex Turbulent Flows and Heat Transfer*. Flow, Turbulence and Combustion, 78(2):177-202, 2007.

[13] Krajnović S. and Helgason E., *LES and PANS, Simulation of Rudimentary Landing Gear - 4 Wheel*. Workshop on Benchmark problems for Airframe Noise Computations – I, Stockholm, Sweden, June 10-11, 2010.

[14] L. Davidson, *Fluid mechanics, turbulent flow and turbulence modeling*, 2011, pp. 138, URL: `http://www.tfd.chalmers.se/~lada/MoF/lecture notes.html`.